

Anisotropy of Nanohertz Gravitational Wave Background and Individual Sources from Supermassive Binary Black Holes Based on Cosmological Simulation

QING YANG,^{1,2} XIAO GUO* ,³ ZHOUJIAN CAO,^{3,4} XIAOYUN SHAO,⁵ AND XI YUAN⁶

¹College of Engineering Physics, Shenzhen Technology University, No.3002 Lantian Road, Shenzhen 518118, China

²Shenzhen Key Laboratory of Ultraintense Laser and Advanced Material Technology, Shenzhen Technology University, No.3002 Lantian Road, Shenzhen 518118, China

³School of Fundamental Physics and Mathematical Sciences, Hangzhou Institute for Advanced Study, University of Chinese Academy of Sciences, No.1 Xiangshan Branch, Hangzhou 310024, China

⁴Institute of Applied Mathematics, Academy of Mathematics and Systems Science, Chinese Academy of Sciences, No. 55 Zhongguancun East Road, Beijing 100190, China

⁵Observatório Nacional, Rio de Janeiro, RJ, 20921-400, Brazil

⁶Department of Physics, Brown University, 182 Hope Street, Providence, 02912, RI, United States

ABSTRACT

Several pulsar timing array (PTA) groups have recently claimed the detection of nanohertz gravitational wave background (GWB), but the origin of this gravitational wave (GW) signal remains unclear. Nanohertz GWs generated by supermassive binary black holes (SMBBHs) are one of the most important GW sources in the PTA band. Utilizing data from cosmological simulation, we construct a comprehensive dataset of SMBBHs within a mock observable universe incorporates the cosmic large-scale structure. We carry out an exhaustive analysis of the distribution characteristics of these merger events, as well as the GWB signals they produce. Specifically, we predict the characteristic amplitude of GWB to be $h_c = 4.85 \times 10^{-16}$ at the frequency of yr^{-1} , while the energy density of GWB signal exhibit an anisotropic part with $C_1/C_0 \approx 2.50 \times 10^{-3} \pm 2.04 \times 10^{-3}$. We study the clustering pattern of the positional distribution of SMBBHs, and found that they show similar behavior with that of galaxies on relatively small scales. Furthermore, for the upcoming Chinese Pulsar Timing Array (CPTA) and Square Kilometre Array (SKA)-PTA, we predict the spatial distribution, numbers and signal-to-noise ratio (SNR) distribution of individual GW sources that may be detected with $\text{SNR} > 8$, and study the anisotropic properties in the spatial distribution of these individual GW sources. We finally investigated the impact of lensing effects and found that their influence is rather limited.

Keywords: black hole physics (159), gravitational waves (678), pulsars (1306), supermassive black holes (1663)

1. INTRODUCTION

Observational data indicates that supermassive black holes (SMBHs) occupy the centers of nearly all massive galaxies (Soltan 1982; Kormendy & Richstone 1995; Magorrian et al. 1998; Yu & Tremaine 2002; Kormendy & Ho 2013). While the precise evolutionary processes behind SMBHs remain unclear, there exist robust correlations between their masses and various observational properties of their host galaxies, encompassing factors such as velocity dispersion, star formation rate, and bulge stellar mass (Madau et al. 1996; Boyle & Terlevich 1998; Magorrian et al. 1998; Ferrarese & Merritt 2000; Ueda et al. 2003; Zheng et al. 2009). Furthermore, it is anticipated that during galaxy mergers, the SMBHs within them will coalesce into supermassive binary black holes (SMBBHs), generating gravitational waves (GW) during their orbital decay and ultimately merge into a single, more massive black hole (Yu & Tremaine 2002; Sesana 2015; Chen et al. 2020; Sah et al. 2024; Sah & Mukherjee 2024). The gravitational torques resulting from these galaxy-galaxy mergers promote the inflow of cold gas towards the galactic centers, igniting central starbursts

* guoxiao@nao.cas.cn

and fuelling accretion onto the SMBHs (Hernquist 1989; Barnes & Hernquist 1991, 1996; Mihos & Hernquist 1994, 1996; Di Matteo et al. 2005). This process of galaxy/SMBH mergers has been proposed as a potential mechanism for activating central active galactic nuclei (AGN) and facilitating the growth of SMBHs (Hopkins et al. 2008; Sanders et al. 1988; Treister et al. 2012).

On the one hand, GWs emitted by numerous inspiraling SMBBHs are anticipated to constitute a GW background (GWB) spanning the frequency range of nHz- μ Hz. The detection of this GWB holds profound and transformative implications for cosmology and galaxy evolution. On the other hand, if GWs emitted from some individual SMBBHs are so strong that they can be detected by GW detectors with significant signal-to-noise ratio (SNR), these GW signals can be resolved as individual GW sources and be separated from GWB.

Precision timing of an ensemble of millisecond pulsars, known as pulsar timing arrays (PTA), offers a unique approach to detect such low-frequency GW signals including GWB and individual sources (Sazhin 1978; Detweiler 1979; Blandford et al. 1984; Foster & Backer 1990; Maggiore 2008; Sesana et al. 2009; Sesana & Vecchio 2010; Creighton & Anderson 2011; Lee et al. 2011; Manchester 2013; Sesana 2013a; van Haasteren 2014; Zhu et al. 2014; Blair et al. 2015; Mingarelli 2015; Schutz & Ma 2016; Taylor et al. 2019). Currently, a diverse array of PTA experiments is operational, including the Parkes PTA (PPTA¹; Manchester 2013), the European PTA (EPTA²; Kramer & Champion 2013), the North American Nanohertz Observatory for Gravitational Waves (NANOGrav³; McLaughlin 2013; Ransom et al. 2019), the Indian Pulsar Timing Array (InPTA; Joshi et al. 2018), the Chinese PTA (CPTA; Nan et al. 2011; Smits et al. 2009), and the MeerKAT PTA (MPTA; Miles et al. 2023). Among which, the first three PTA groups have amassed data spanning over a decade in pursuit of potential low-frequency GW signals. They have also collaborated to form the International PTA (IPTA⁴; Manchester & IPTA 2013; Brazier et al. 2016; Perera et al. 2019) by sharing data. Looking forward, the Square Kilometer Array (SKA) (e.g., Lazio 2013; Wang & Mohanty 2017) is anticipated to discover numerous stable millisecond pulsars (MSPs) and establish a high-sensitivity PTA, henceforth referred to as SKA-PTA, to detect low-frequency GW sources. Recently, CPTA, NANOGrav, EPTA (+InPTA), and PPTA have presented evidence for the presence of a nanohertz GWB with a confidence level of approximately 2-4 σ (Xu et al. 2023; Agazie et al. 2023a; Reardon et al. 2023; EPTA Collaboration et al. 2023) (see also Arzoumanian et al. 2020). Although the origin of this GWB is still unclear, it is likely that this signal can be attributed to, or at least partly attributed to GWs generated from cosmic inspiraling SMBBHs, indicating that the detection of individual SMBBHs may also soon become a reality (e.g., Chen et al. 2023; Agazie et al. 2023b; Antoniadis et al. 2023).

In recent years several studies have also presented predictions on this GWB based on phenomenological models or simulations (Jaffe & Backer 2003; Sesana 2013b; Sesana et al. 2016; Kelley et al. 2017; Yang et al. 2019). The predicted GW strain amplitude ($A_{\text{yr}^{-1}}$) lies approximately within the range of 1×10^{-16} to 5×10^{-15} . The practical GW strain amplitude ($A_{\text{yr}^{-1}}$) from GWB detected by NANOGrav, CPTA, EPTA and PPTA is around 2×10^{-15} . The predictions regarding the characteristic amplitude of the GWB focus on its isotropic nature, which represents an ideal scenario when the sources of the GWB are extremely numerous that their distribution are nearly continuous, and resulting in the predicted characteristic Hellings and Downs curve that could be observed in PTA experiments (Hellings & Downs 1983). However, in reality, the number of SMBBHs is finite, leading to a GWB signal comprising both a dominant isotropic component and also anisotropic contributions. The impact of anisotropies on PTA measurements and the extension of the Hellings and Downs curve method to analyze anisotropies in the GWB have been explored in various studies, including Cornish & Sesana (2013); Mingarelli et al. (2013); Taylor & Gair (2013); Cornish & van Haasteren (2014); Mingarelli (2015); Hotinli et al. (2019); Sato-Polito & Kamionkowski (2024). Several PTAs have also provided constraints on the level of anisotropy in the GWB (Taylor et al. 2015).

Although there has been some work exploring the anisotropy property of the GWB signal (Yang et al. 2019; Sato-Polito & Kamionkowski 2024), they usually rely on randomly distributed SMBBHs without considering the possible effects of the large-scale structure of the universe. The method we use allow us to estimate the anisotropy of GWB in a simulation environment where the cosmic large scale structure is incorporated, thus more reflective to the real universe and offering a more reliable result. In this paper, we intend to employ a semi-analytic galaxy formation model (SAM) grounded on dark matter (DM) halo merger trees derived from the Millennium simulation (Springel et al. 2005; Guo et al. 2011). We will focus on the MR model, specifically the variants proposed by Guo et al. (2011, 2013)

¹ <http://www.atnf.csiro.au/research/pulsar/ppta/>

² <http://www.epta.eu.org/>

³ <http://nanograv.org/>

⁴ <http://www.ipta4gw.org/>

(see also [Henriques et al. 2015](#)), to construct a comprehensive dataset of SMBBHs within a mock observable universe, from which we forecast the formation rate of SMBBHs, their statistical properties regarding redshifts, mass and mass ratios, their spatial and angular distributions, and the characteristic strain amplitude of the resulting GWB, along with its anisotropic characteristics. We conduct a detailed study on the three dimensional spatial and two dimensional angular distributions of GW sources with the SMBBHs that we constructed in the observable universe, and present the resulting angular power spectrum coefficients and angular two-point correlation functions. We also predict resolvable individual GW sources for future CPTA and SKA-PTA, and show their statistical properties. In addition, we will also make an estimation on how gravitational lensing effect will affect all of our calculational results.

This paper is organized as follows. In Section 2, we introduce the galaxy evolution model and mock data we used, as well as the basic setups and methods for constructing SMBBHs in the observable universe. In Section 3, we present our basic results concerning the isotropic and anisotropic characteristics of the GWB signal, which we derived from the SMBBH data constructed, and also the clustering properties of the GW sources. We further discuss the detection capabilities of different PTAs for individual bright sources in Section 4. In Section 5, we take into account the effects of gravitational lensing and discuss their impact on all of our calculational results derived above. Finally, Section 6 is devoted to conclusions and discussions. Throughout this paper, we adopt that dimensionless Hubble constant $h_0 = 0.704$.

2. MODELS

In this section, we introduce how we construct the light cone SMBBH data in the observable universe. The flowchart of the entire process to deal with simulation data and generate simulated GW sources is shown in Figure 1. We will introduce our method related to each part of the flowchart in detail in the following subsections.

2.1. Mock Data

We utilize the results of L-Galaxies semi-analytical galaxy formation runs using the model described in [Guo et al. \(2011, 2013\)](#) stored in the Millennium simulation database Guo2013a. This is a semi-analytical modelling applied to the DM halo merger trees of the Millennium simulations, which follows the formation, evolution and mergers of galaxies in a box with side length of $500 \text{ Mpc}/h_0$ from $z > 14$ to $z = 0$. Since SMBH and galactic nuclear activity is closely related to galaxy formation, SAM always encompass the growth and evolution of SMBHs in their modeling. In Guo2013a, “quasar” mode and “radio” mode are considered to grow SMBHs from initial seeds, leading to a co-evolution of SMBHs and their host galaxies that is compatible with observations. We assume that SMBHs will form inspiring binaris following the merger of their host galaxies, so according to the merger history of DM halos and galaxies from Guo2013a simulation result, we can judge when and where a SMBBH will form. In this way, we get the SMBBH merger events distributed in one simulation box, each event carries information including their locations in the simulation box, redshifts, host galaxies, progenitor black hole masses and descendant black hole mass.

2.2. Observable Universe

The mock simulation data are output in 61 snapshots at different redshifts in a box with side length $500 \text{ Mpc}/h_0$. However, instead of SMBBHs at specific redshifts in a box with limited size, signals observed by PTA originate from SMBBHs distributed along the light cone, with larger distance to us at higher redshifts. These SMBBHs constitutes the observable universe centered at the earth, and the distance of them may exceed the side length of the simulation box at relatively high redshifts. In order to construct this observable universe with mock data, and considering the universe is uniform and isotropic on large scale ($> 100 \text{ Mpc}$), we adopt periodic boundary conditions, i.e., we piece together the simulation box in a repeating pattern to generate a universe that can theoretically stretch out indefinitely in all three directions. We set the position of the observer to be at the origin, which is a vertex of the simulation box with coordinates $(0,0,0)$, e.g., see the blue sphere in Figure 2 and Figure 7. For each redshift snapshot, we calculate the corresponding comoving distance. We then draw a spherical shell at this distance with certain thickness, which we chose to be the comoving distance difference between neighboring redshifts. Any SMBBH event that falls within the shell corresponds to its redshift is considered to be within the light cone and are saved as observable GW source events. In Figure 2, we illustrate this process for the initial three redshift snapshots. A gentle reminder is that we fully utilized the total 61 redshift snapshots in our analysis instead of the initial three as depicted in the figure.

2.3. GW Sources

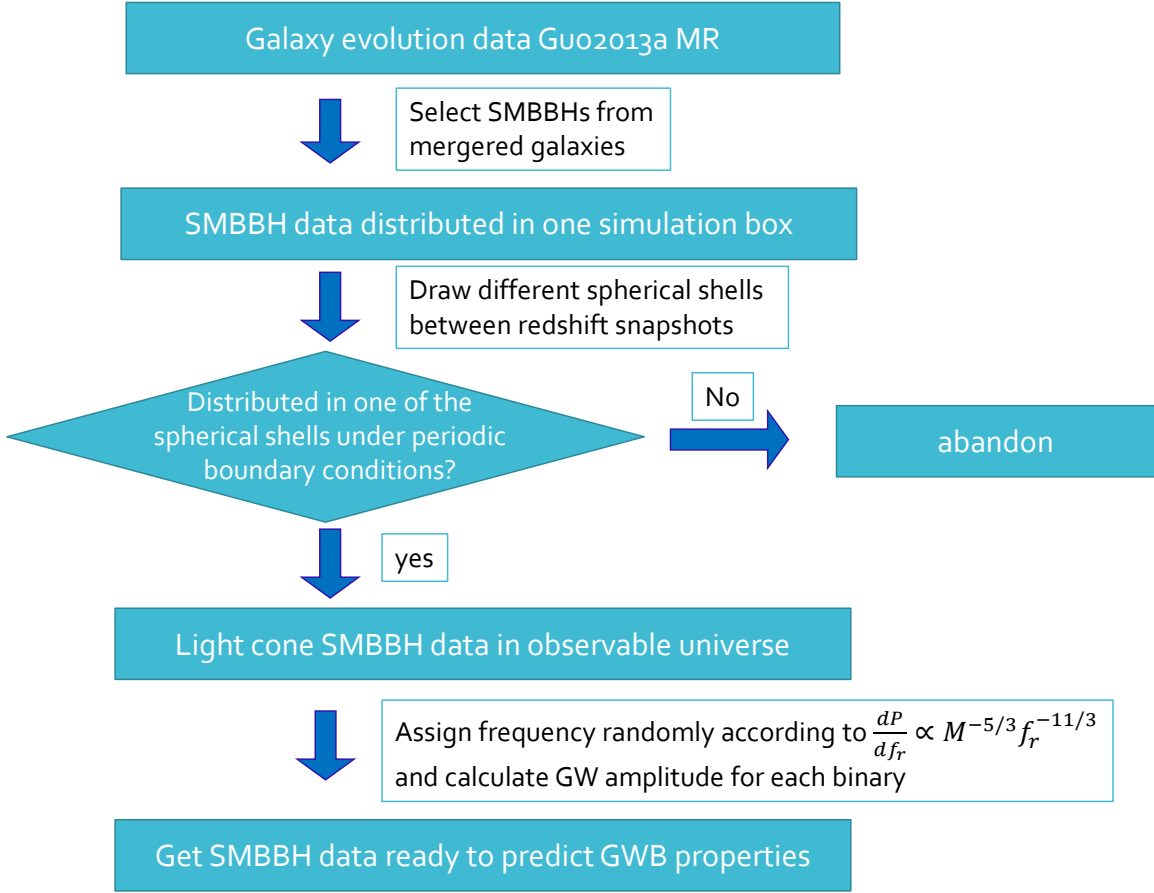


Figure 1. A flowchart for constructing GW events in the observable universe from Guo2013a MR mock data.

We ultimately obtained $N_{\text{total}} \approx 3.027 \times 10^7$ SMBBH events in the observable universe with methods described in the previous subsection. We consider these SMBBHs to serve as GW sources whose signals could be detectable in the PTA frequency band. To predict the characteristics of the GWB signal from these GW sources, we still need to determine the GW strain and frequency for each SMBBH events, the method is described below.

2.3.1. GW Strain

Given that the pulsars utilized by PTA may be situated at various locations with diverse inclinations, the orientation of the PTA itself can be considered arbitrary. Furthermore, the SMBBHs under observation can also exhibit a wide range of inclinations. Hence we adopt the following formula to estimate the average GW strain for each SMBBH:

$$h = \sqrt{\frac{32}{5} \frac{G^{5/3} \mathcal{M}_z^{5/3} (\pi f_{\text{obs}})^{2/3}}{c^4 d_L}}, \quad (1)$$

where d_L is the luminosity distance of GW source, $\mathcal{M}_z = \mathcal{M}(1+z)$ is the redshifted mass, with chirp mass $\mathcal{M} = \frac{(m_1 m_2)^{3/5}}{M^{1/5}}$, and m_1, m_2 are the masses of the two components of this SMBBH, $M = m_1 + m_2$ is the total mass of this SMBBH. Observational frequency $f_{\text{obs}} = \frac{f_r}{1+z}$, where f_r is the GW frequency in the rest frame of GW source. Here we assume the orbit of each SMBBH is circular for simplicity. As for how the GW frequency is generated is described in the next subsection.

2.3.2. Frequency Generating

The PTA sensitive frequency range is limited by two parameters: observational duration T_{obs} and observational cadence Δt . Under these two parameters the detectable frequency range can be determined as $\frac{1}{T_{\text{obs}}} < f_{\text{obs}} < \frac{1}{\Delta t}$.

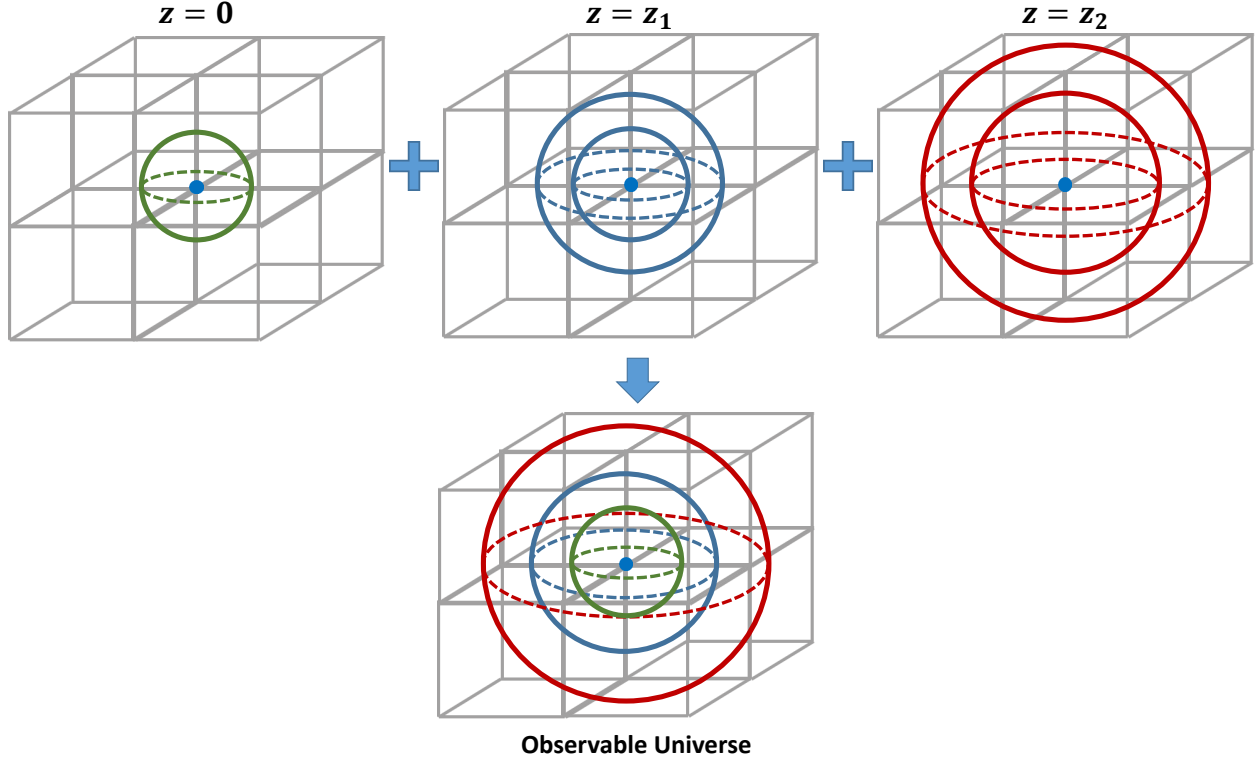


Figure 2. An illustration of constructing the observable universe using periodic boundary conditions for the initial three redshift snapshots. The upper three plots represent the periodic simulation boxes of the initial three redshift snapshots respectively. The spherical shells representing the extent of the light cone are shown in each plot. SMBBHs that fall within these shells are selected as light cone events. By collecting the light cone events from different redshifts, the observable universe is constructed.

When considering an observational duration of a few decades, the lower limit of the frequency band is approximately 10^{-9} Hz. The frequencies of the GW signals from individual sources are determined by a variety of factors, including the orbital separation of the two black holes, their individual masses, the redshift of the source, and so on. Mock data from SAM do not contain these information, so we need to assign frequencies to each SMBBH system randomly. We adopt the quadrupole approximation, according to which the residual time within a unit logarithmic frequency interval is given by (Maggiore 2008)

$$\frac{dt_r}{d \ln f_r} = \frac{5}{96} \pi^{-8/3} \left(\frac{GM}{c^3} \right)^{-5/3} f_r^{-8/3}. \quad (2)$$

We assume that the probability of a SMBBH system being at a certain orbital frequency is directly proportional to the residual time, thus the probability distribution of the rest frame GW frequency from BBH merger is

$$P(\ln f_r) = \frac{dP}{d \ln f_r} \propto \mathcal{M}^{-5/3} f_r^{-8/3}, \quad (3)$$

or

$$\frac{dP}{df_r} \propto \mathcal{M}^{-5/3} f_r^{-11/3}. \quad (4)$$

We restrict the distribution of f_r to be between f_0 and f_{ISCO} , where $f_0 = 10^{-9}$ Hz is roughly the lower limit of PTA frequency band and f_{ISCO} is the GW frequency when the SMBBH system is at the inner-most stable circular orbit. f_{ISCO} may vary among different SMBBH systems. We calculate f_{ISCO} as follows: According to Kepler's third law, $GM = a^3 \omega_{\text{orb}}^2 = \pi^2 a^3 f_r^2$ with M the total mass, for spinless SMBBH, the radius of the inner-most stable circular orbit $a = \frac{6GM}{c^2}$, thus GW frequency from this orbit is given by (Maggiore 2008; Sathyaprakash & Schutz 2009):

$$f_{\text{ISCO}} = \frac{c^3}{\pi 6^{3/2} GM} \approx 4.4 \times 10^{-7} \text{ Hz} \left(\frac{10^{10} M_{\odot}}{M} \right). \quad (5)$$

According to the probability distribution of Eq. (4), we randomly generate frequency for each of the GW sources (see also Figure 5) with Monte Carlo method.

3. RESULTS

With methods described in Section 2, we produced $N_{\text{total}} \approx 3.027 \times 10^7$ light cone SMBBH GW sources distributed in the observable universe. Each binary system has a distinct location, redshift, binary black hole masses, and gravitational wave frequency. We superimposed the gravitational wave signals from these binary black hole systems to obtain the GWB signal and studied its properties. In this section, we will present the basic characteristics of the SMBBH mock data we have obtained, as well as our main results for the GWB signal.

3.1. Statistical Properties of Light Cone SMBBH Mock Data

We present the basic statistical properties of our light cone SMBBH mock data in this subsection. The total mass M (left panel) and mass ratio q (right panel) distributions of the SMBBHs are demonstrated in Figure 3. The total masses of the binary systems are basically between $10^6 M_{\odot}$ and $10^{9.5} M_{\odot}$ and peak around $5 \times 10^7 M_{\odot}$. On the other hand, the mass ratio distribution of the SMBBHs generally exhibits a monotonically decreasing trend with increasing mass ratio q , the vast majority of the binary black hole systems have mass ratios below 0.4, and even close to zero. This indicates that in our data, the majority of the binary black hole systems exhibit a significant difference in mass between the two black holes. The redshift distribution of the SMBBHs is shown in Figure 4. This distribution peaks around redshift $z \sim 1.1$, and the maximum redshift can reach $z = 6.5$.

The frequency distribution of the GW signals from our SMBBH systems, including rest frame frequency f_r and observed frequency f_{obs} , are shown in Figure 5. They basically follow the power law distribution as expected from Eq. (4). Since f_{obs} is the redshifted f_r , so we usually have $f_{\text{obs}} < f_r$, we can see from the figure that the distribution range of f_{obs} is correspondingly lower.

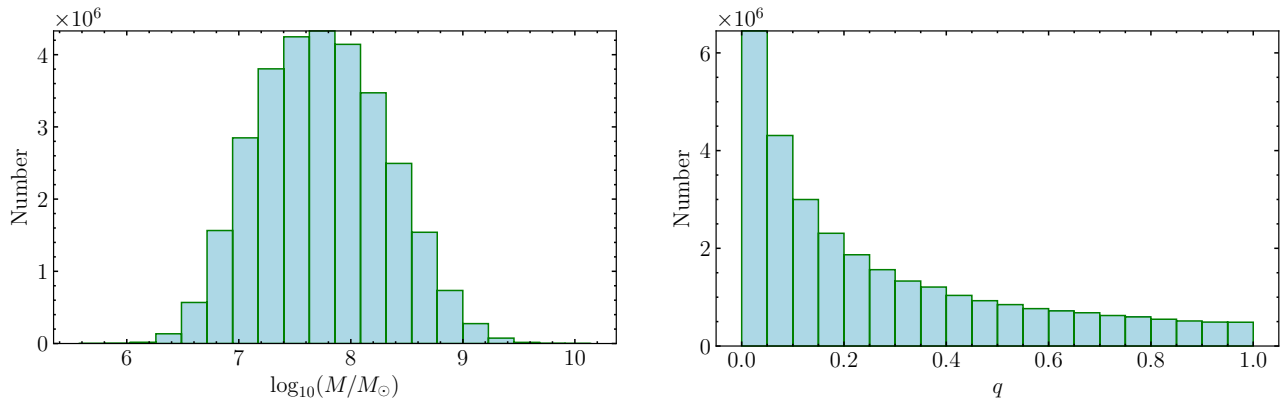


Figure 3. The total mass M (left) and mass ratio q (right) distribution of the light cone SMBBHs.

3.2. Isotropic Part of the Simulated GWB Signal

Unlike a series of earlier studies which relied on the estimation of SMBBH merger rate to deduce the characteristic amplitude of the GWB signal, our methodology incorporates a vast amount of individual sources scattered across the observable universe to construct GWB. From the green curve in Figure 5 we can see that, The observable frequency range of our GWB signal is roughly between 10^{-10} Hz to 10^{-6} Hz. Considering 10^{-10} Hz is already below the lower frequency limit of the PTA band. We will primarily analyze the behavior of the resulted GWB signal between 10^{-9} Hz to 10^{-6} Hz.

To calculate the resulting monopole part of the GWB signal and its characteristic strain spectrum, we divide $\ln f$ into $N_{\text{bin}} = 10$ bins in the range 10^{-9} Hz to 10^{-6} Hz, and select those SMBBHs whose observed frequencies are within the specified range in each bin. The resulting GW characteristic strain near a certain frequency can be calculated as a summation of strains from selected individual GW sources in the respective bin divided by the bin width, which can

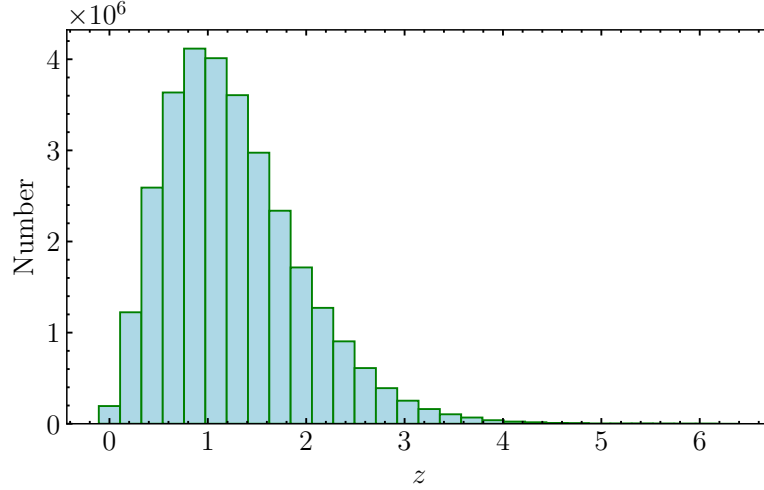


Figure 4. The redshift distribution of the light cone SMBBHs. The distribution peak at around $z \sim 1.1$, while the maximum redshift is 6.2.

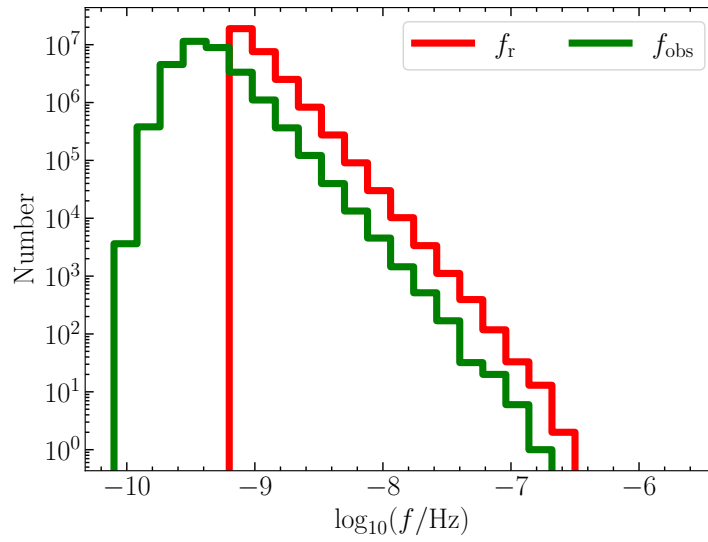


Figure 5. The frequency distribution of the GW sources, red: rest frame frequency f_r ; green: observed frequency f_{obs} . They basically follow power law behavior as expected. The distribution range of $f_{\text{obs}} < f_r$ is relatively lower due to redshift.

be expressed as:

$$h_c(f_j) = \sqrt{\sum_{\ln f_j - \frac{\Delta \ln f}{2} < \ln f_i \leq \ln f_j + \frac{\Delta \ln f}{2}} \frac{h_i^2}{\Delta \ln f}},$$

where $\Delta \ln f = \frac{f_{\text{max}} - f_{\text{min}}}{N_{\text{bin}}}$, and h_i can be computed according to Equation (1). We present our results regarding the characteristic strain spectrum of GWB in Figure 6. In this figure, we also indicated the data points at the characteristic frequency of yr^{-1} with the presupposed $-\frac{2}{3}$ power-law spectrum from the latest NANOGrav (Agazie et al. 2023a), EPTA (EPTA Collaboration et al. 2023) and CPTA (Xu et al. 2023) results. From the figure we can see that, our results generally exhibit the characteristic $-\frac{2}{3}$ power-law dependence. In the high-frequency region, the curve drops slightly, which can be easily understood as the frequency upper limit f_{ISCO} is different from event to event,

according to Eq. (5), only events with small total mass can reach a relatively high signal frequency. This will lead to a decrease in the number of events in the high-frequency bins and a deviation from the $-2/3$ power-law behavior in the characteristic strain spectrum. On the other hand, it is easily noted that our curve lies below the observational results which have $A_{\text{yr}^{-1}} \approx 4.85 \times 10^{-16}$ at $f = 1\text{yr}^{-1}$. We will discuss this point in the discussion section. Nevertheless, the projected value resides well within the theoretical range $[1 \times 10^{-16}, 5 \times 10^{-15}]$, as supported by existing literature.

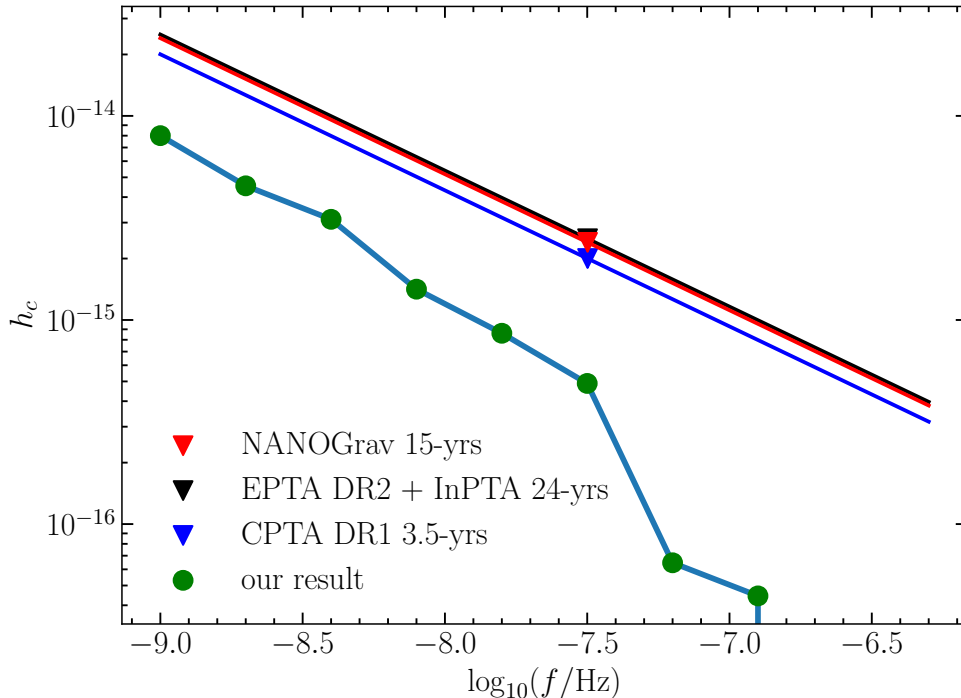


Figure 6. The characteristic strain spectrum of GWB signal from our light cone mock data (green points). The latest results from NANOGGrav (Agazie et al. 2023a), EPTA (EPTA Collaboration et al. 2023) and CPTA (Xu et al. 2023) at the characteristic frequency of yr^{-1} are also shown.

3.3. Anisotropy

Now we study the anisotropy properties of the GWB signal we get from our mock data, which is a result of GW sources and the GW strains come from them not being distributed isotropically in the virtual observable universe. The method we use allow us to estimate the anisotropy of GWB in a simulation environment more reflective to the real universe, as the cosmic large scale structure is incorporated. In this subsection, we will present how the sources in our simulation data are distributed across the observable universe and demonstrate the resulting anisotropic characteristics of the GWB signal.

3.3.1. Spatial Distribution of GW Sources

As mentioned previously, we obtain $N_{\text{total}} \approx 3.027 \times 10^7$ SMBBH GW sources in total. Due to the exceedingly large number, it is impractical to represent all of them in the figure. Thus we show the $\frac{1}{8}$ -cube three dimensional spatial distribution of GW sources with side length 500 Mpc in Figure 7, and its two dimensional projection in Figure 8. It can be seen from the figures that the supermassive black holes we constructed extended from the earth position to comoving distance beyond 8000 Mpc, corresponding to redshift from 0 to over 6. Similar patterns to the “cosmic web” can be recognized from the figures, demonstrating that supermassive black holes may also carry information about the large-scale structure of the universe Shao et al. (2022); Zheng et al. (2023); Li et al. (2024), we will discuss this point in subsection 3.3.3.

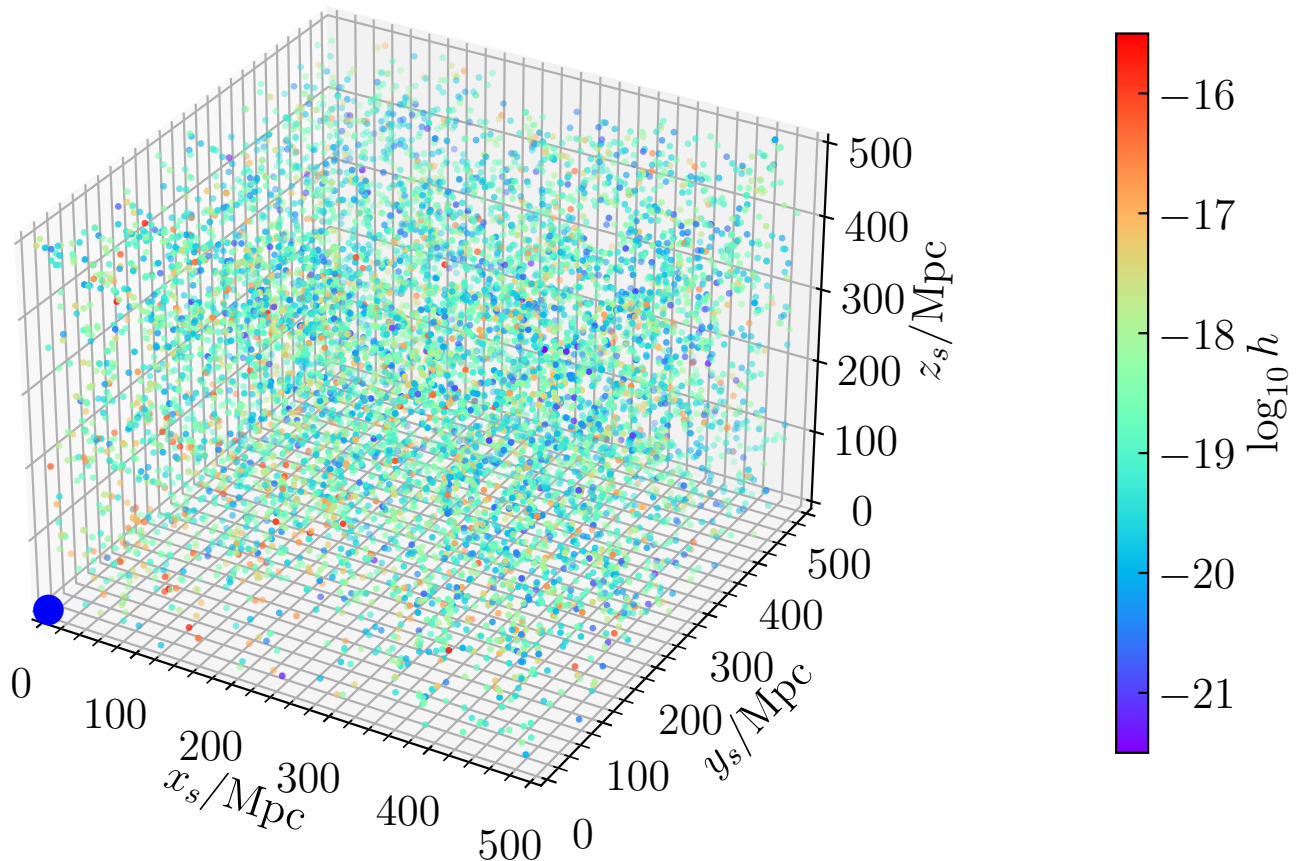


Figure 7. The three dimensional spatial distribution of GW sources whose locations are within the box of side length 500Mpc ($0 < x_s, y_s, z_s < 500$ Mpc). Here we only show 1/8 part of the observable universe we constructed. We use colors to represent the GW amplitude of each source, we also mark the Earth's position in the figure with a large blue sphere. From the figure we can distinguish the distribution patterns of cosmic large-scale structures such as voids and clusterings to a certain degree.

3.3.2. Angular Power Spectrum

We transform the three dimensional Cartesian coordinates (x_s, y_s, z_s) of the mock SMBBH locations to spherical polar coordinates (r, θ, ϕ) , where $r = \sqrt{x_s^2 + y_s^2 + z_s^2}$, ϕ represents right ascension (the azimuthal angle respective to x_s -axis positive direction), and θ represents declination (elevating angle respective to $x_s O y_s$ plane). By superimposing the gravitational wave signals from all possible sources along a particular direction, we obtain a background gravitational wave signal sky map distributed across the celestial sphere. In Figure 9, we show the resulted sky map for GW strain $h(\hat{\Omega})$. Since energy density $\rho(\hat{\Omega})$ is proportional to the squared strain $h^2(\hat{\Omega})$, the sky map of energy density will be similar to the strain map, with the value of each pixel squared.

Similar to Yang et al. (2019); Taylor & Gair (2013), we use spherical harmonic analysis to quantitatively analyze the anisotropy properties of the GWB signal from mock SMBBHs. The GW energy density $\rho(\hat{\Omega})$ can be expanded under the spherical harmonic basis:

$$\rho(\hat{\Omega}) = \sum_{l=0}^{\infty} \sum_{m=-l}^l c_{lm} Y_{lm}(\hat{\Omega}), \quad (6)$$

where the coefficient c_{lm} can be calculated as:

$$c_{lm} = \int d\hat{\Omega} \rho(\hat{\Omega}) Y_{lm}(\hat{\Omega}). \quad (7)$$

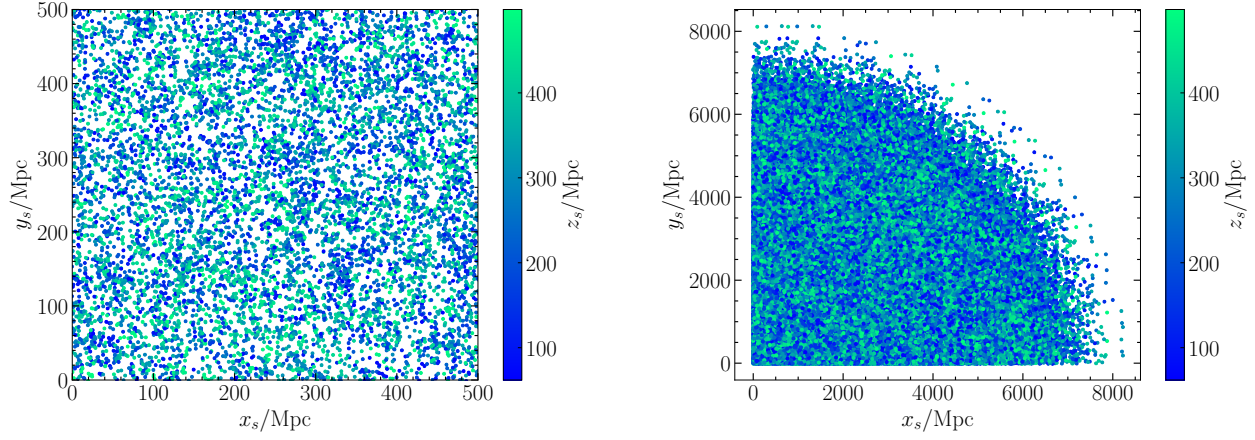


Figure 8. Left: The two dimensional projection of the three dimensional spatial distribution shown in Figure 7. Here we use colors to represent the coordinate z_s of the GW sources. We can also distinguish void regions and fibrous structures from the figure.

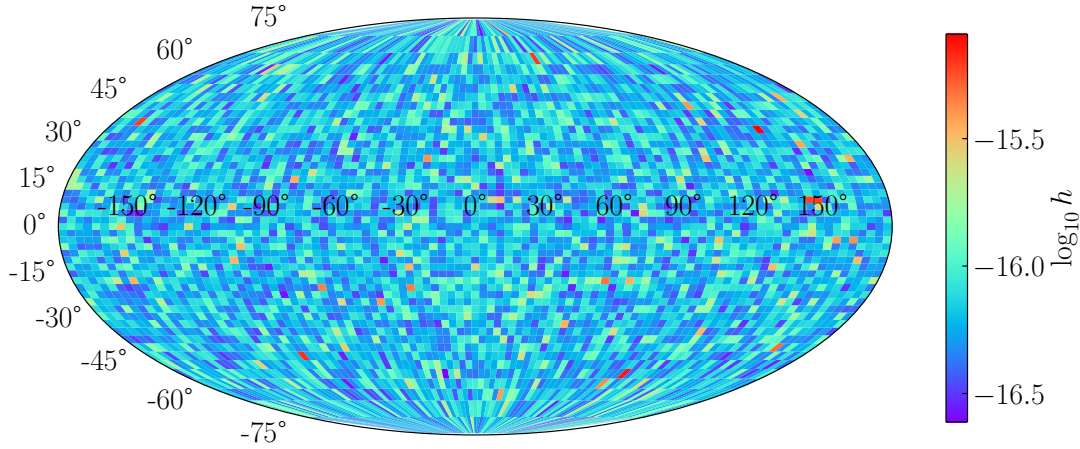


Figure 9. The sky map of GWB strain $h(\hat{\Omega})$ across the celestial sphere. Since energy density is proportional to $h^2(\hat{\Omega})$, it will follow similar sky map with each value on the sphere squared.

In practical, we divided the celestial sphere into N small regions to perform the superposition of GW signals in a specific direction, so the integral above should be replaced with a summation:

$$c_{lm} = \sum_{i=1}^N \rho(\hat{\Omega}_i) Y_{lm}(\hat{\Omega}_i) \frac{4\pi}{N}. \quad (8)$$

Then the angular power spectrum can be expressed as an average of all $|c_{lm}|^2$ with the same l as:

$$C_l = \sum_{m=-l}^l \frac{|c_{lm}|^2}{2l+1}.$$

and the estimated error of each coefficient C_l from cosmic variance is (Bartolo et al. 2022):

$$\Delta C_l = \sqrt{\frac{2}{2l+1}} C_l. \quad (9)$$

To calculate the coefficients C_l for GW strain h , we just substitute energy density $\rho(\hat{\Omega})$ with strain $h(\hat{\Omega})$ in Equation (6), (7) and (8).

Based on these formulas, we calculated the angular power spectrum for the GWB energy density $\rho(\hat{\Omega})$. In Figure 10, we show the resulted C_l 's as a function of l . We can see that, $C_1/C_0 \approx 2.50 \times 10^{-3} \pm 2.04 \times 10^{-3}$ and $C_2/C_0 \approx 2.48 \times 10^{-3} \pm 1.57 \times 10^{-3}$, and higher-order C_l/C_0 values generally fluctuate within the range of 0.001 to 0.003. The behavior of the C_l coefficients from energy density resides well within the observational constraints, i.e., $C_{l>0}/C_{l=0} < 20\%$ (Agazie et al. 2023c). Fluctuations in the ratio C_l/C_0 across different values of l may suggest the presence of clustering patterns in the spatial scale correspond to each specific l , and may indicate the existence of underlying structures in the angular distribution of the background GW strains. In Figure 11, we also plotted the C_l coefficients in different frequency bins as shown in its legend. It can be seen from the figure that the ratio C_l/C_0 differ significantly across different frequency bins, and general increase with increasing frequency, this can be understood because as the frequency increases, the number of SMBBHs decreases, leading to an increase in anisotropy. C_1/C_0 at higher frequency end can even reach ~ 0.8 . When $l \gg 1$, $C_l/C_0 \simeq 0.6$ at high frequency end around $\sim 10^{-6}$ Hz. While in the lower frequency end, C_l/C_0 ranges from 0.001 to 0.01 for $l > 0$. The total anisotropy mainly depends on lower frequency end around $\sim 10^{-9}$ Hz.

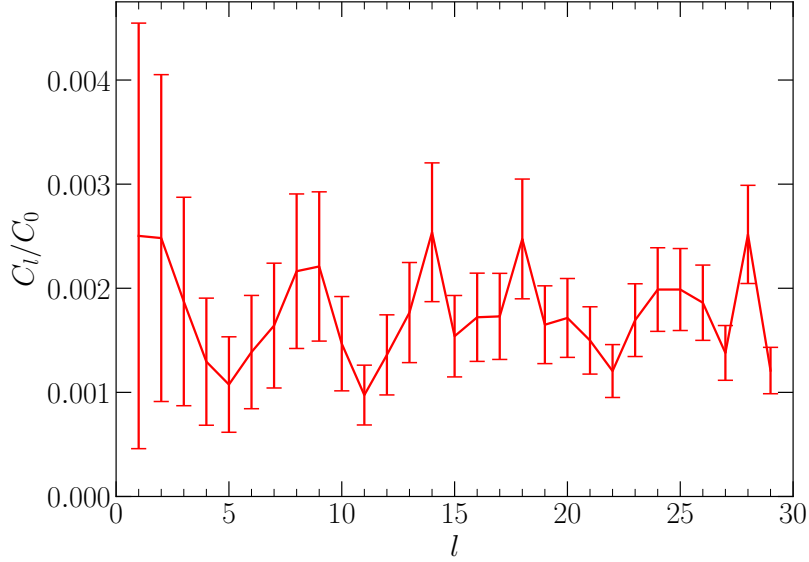


Figure 10. The angular power spectrum coefficients C_l as a function of l for GWB energy density ρ , where error bar indicate the cosmic variance.

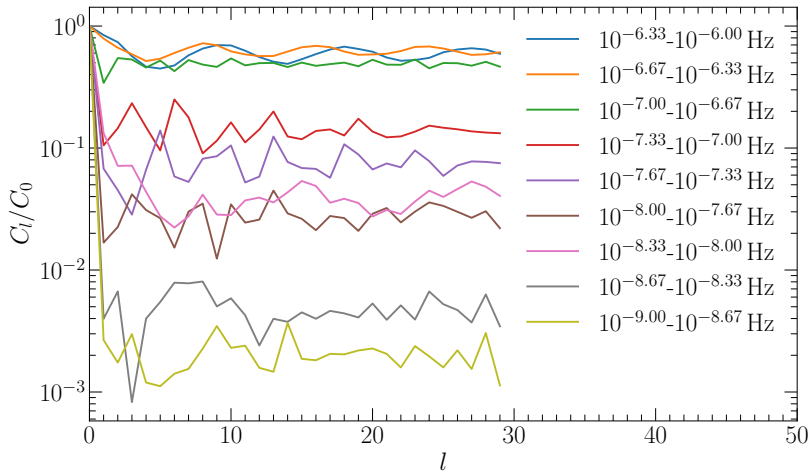


Figure 11. The angular power spectrum coefficients C_l as a function of l for GWB energy density ρ in different frequency bins.

3.3.3. GW Sources in a Shell

We are interested in whether the distribution of SMBBHs can reproduce the large-scale structure of the universe, and thus be used for cosmological purpose like galaxies. Given that the GW sources are situated at different distances from us, it is difficult to determine the physical scale corresponding to specific angular scales. To better study the clustering patterns exhibited in the spatial distribution of the GW sources from angular power spectrum, we selected GW sources located in different spherical thin shells with radius from $R-dR$ to $R+dR$, where we choose $dR = 10$ Mpc and radius $R=382, 764$ and 1528 Mpc, which corresponds to redshift $z = 0.09, 0.19$ and 0.41 respectively. Figure 12 shows the angular position distribution sky map of these GW sources in the three different spherical shells (from top to bottom). As the radius of the spherical shell increases, more and more SMBBHs gather within the range of the shell, thus appearing increasingly crowded. In Figure 13 we also plotted a small patch of the celestial sphere, where we simultaneously displayed the distribution of SMBBHs and background galaxies. The distribution of SMBBHs is sparser than that of galaxies, particularly in spherical shells with smaller radius. It appears that SMBBHs alone may only provide incomplete information about the large-scale structure of the universe.

In order to make a quantitative estimation about to what extent could the distribution of SMBBHs trace the underlying matter distribution of the universe, we calculated the C_l coefficients for the number density of both GW sources and galaxies in these spherical shells and show the results in Figure 14. Different l corresponds to different angular scale α based on the relationship $\alpha = \frac{\pi}{l}$. When the radius R of the spherical shells is fixed, a certain angular scale α corresponds to a specific physical scale $R\alpha$. We observe that, compared to SMBBHs, the C_l/C_0 values of galaxy distribution exhibit more significant fluctuations when l is relatively small, which indicates the stronger clustering of galaxies on large scales. In contrast, C_l/C_0 of SMBBH distribution show less variation within the corresponding range. On the other hand, the behavior of C_l/C_0 of both galaxies and SMBBHs gradually converges as l increases. This indicates that only on relatively smaller scales, the distribution of SMBBHs may exhibit similar patterns to that of galaxies.

We further calculated the angular two point correlation function $\omega(\alpha)$ in these three shells as defined by the following formula:

$$\omega(\alpha) = \frac{DD(\alpha) - 2DR(\alpha) + RR(\alpha)}{+RR(\alpha)}. \quad (10)$$

where $DD(\alpha)$ and $RR(\alpha)$ correspond to the number of SMBBH or galaxy pairs with angular separation α in data-data and random-random catalogs, respectively, whereas $DR(\alpha)$ corresponds to the number of pairs with separation α calculated between data and random catalogs. The results are shown in Figure 15. In the figures, we observe that the angular correlation functions exhibit similar trends to those of the angular power spectra. For smaller spherical shells and smaller angular ranges, the correlation functions of SMBBHs and galaxies are relatively close to each other. However, for larger spherical shells or larger angles, the correlation functions of the two show significant deviations, where the correlation of galaxies is stronger than that of SMBBHs on the corresponding angular scales. This is understandable, because as can be clearly seen from Figure 12 and Figure 13, the distribution of SMBBHs is more homogeneous than that of galaxies. Therefore, they can only reproduce the clustering pattern of galaxies on small scales, while the more densely populated regions of galaxies on large scales are not reflected in the distribution of SMBBHs.

Of course, these are ideal theoretical discussions within the simulated universe. In reality, we need to be able to distinguish these SMBBHs and their angular positions on the celestial sphere. With the improvement of experimental techniques in the future, we will be able to detect an increasing number of individual sources, by combining them with the distribution of stellar-mass black hole events, and calculate their correlation functions or cross-correlations functions with galaxies, the clustering properties of binary black hole events still hosts the possibility to provide us with useful information across larger scale ranges.

4. DETECTABILITIES

4.1. Individual Sources

In the previous analysis, we assumed that the superposition of GW signals emitted by all SMBBH systems within the simulated light cone together form the GWB signal, which is correct for current PTAs. Actually, some individual GW sources can be detected by more powerful PTAs with enough SNR ρ ($\rho > 8$) in the future. So these individual GW sources can be resolvable and separated from background. For future CPTA and SKA-PTA featuring greater detection capability and higher accuracy (The parameters related to their experimental configurations are presented in Table 1),

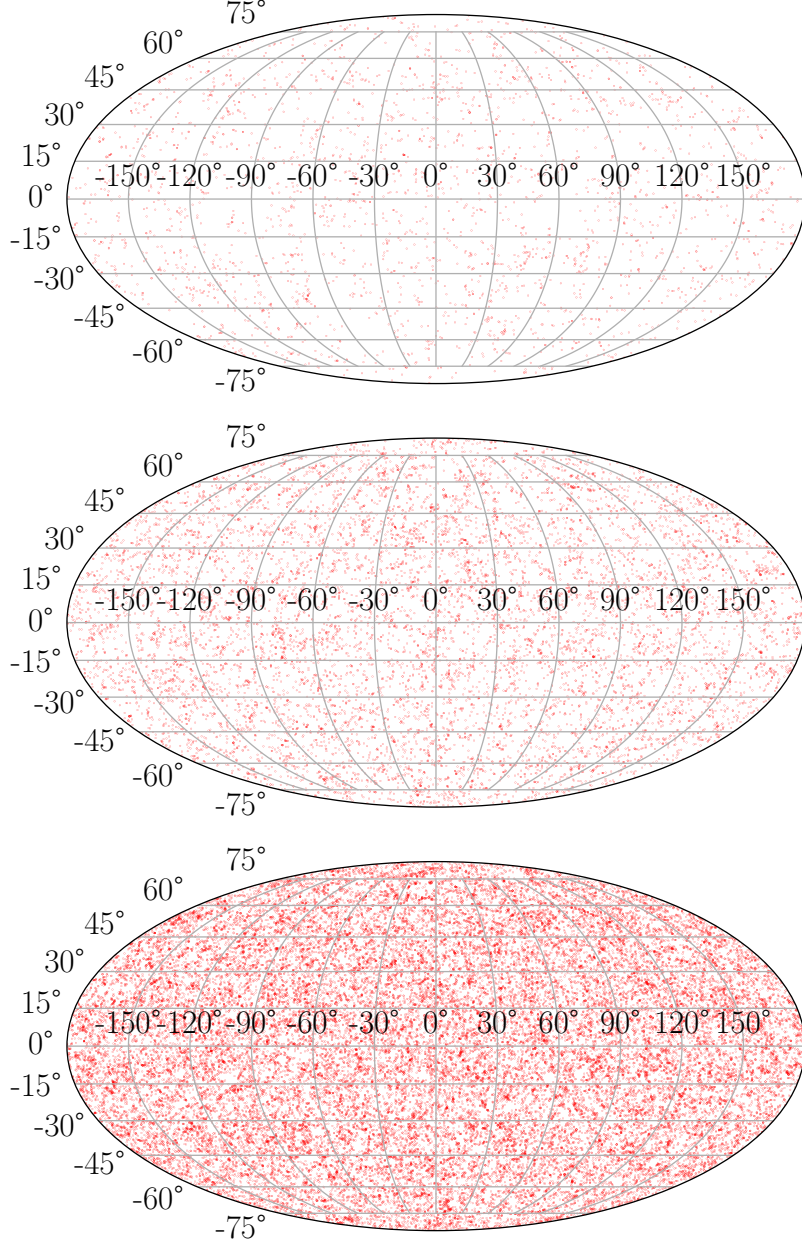


Figure 12. The angular distribution sky map of GW sources in spherical shells with radius $R = 382, 764$ and 1528 Mpc, respectively (from top to bottom), where red point represents the position of each GW source.

Table 1. Parameter settings for two PTAs. Columns from left to right denote the notation of the PTA, total number of MSPs monitored by the PTA N_p , the timing precision σ_t , the total observational period T_{obs} and the mean cadence Δt (Guo et al. 2022; Chen et al. 2023; Guo et al. 2024).

PTAs	N_p	σ_t (ns)	T_{obs} (yr)	Δt (yr)
CPTA	100	20	20	0.04
SKA-PTA	10^3	10	20	0.04

assuming a 20-years' observation period, we calculated the SNR of our sampling SMBBHs based on Equation (85)

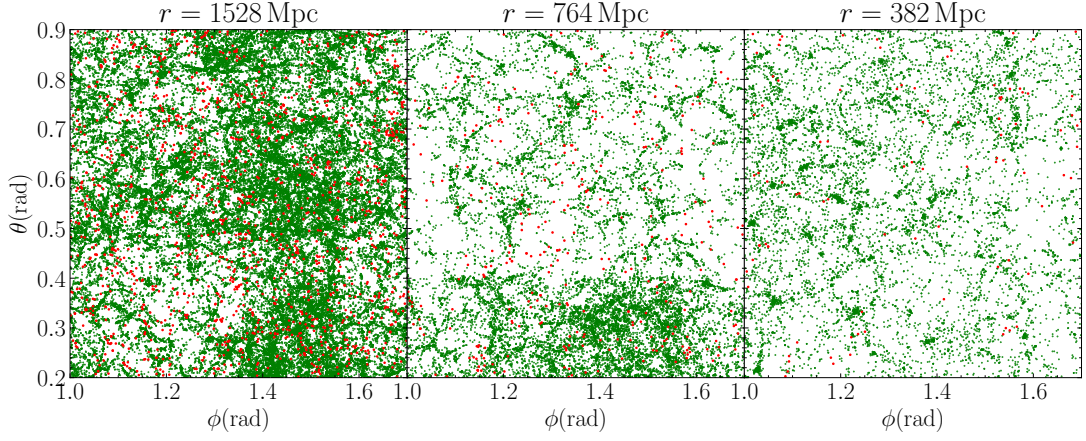


Figure 13. A small portion of the sky map with both GW sources and galaxies in spherical shells with radius $R=1528$, 764 and 382 Mpc, respectively (from left to right). The red points represent the positions of SMBBHs, while the green points represent the positions of galaxies.

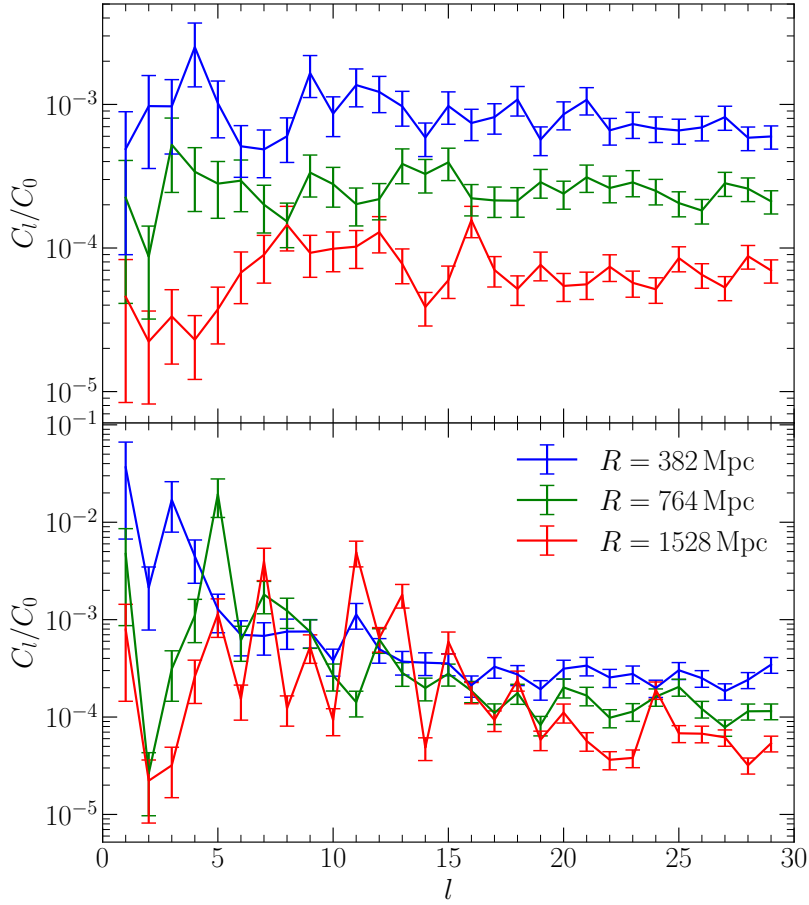


Figure 14. Angular power spectrum coefficients C_l as a function of l for the number density of GW sources (top) and galaxies (bottom) in different spherical shells.

in Guo et al. (2022), and selected those GW sources that can be resolved by these future PTAs. We show the three dimensional spatial distribution of these selected individual sources in Figure 16 for both CPTA and SKA-PTA, where we also use colors to represent the SNR of each source. Our results suggest that, future CPTA is projected to detect

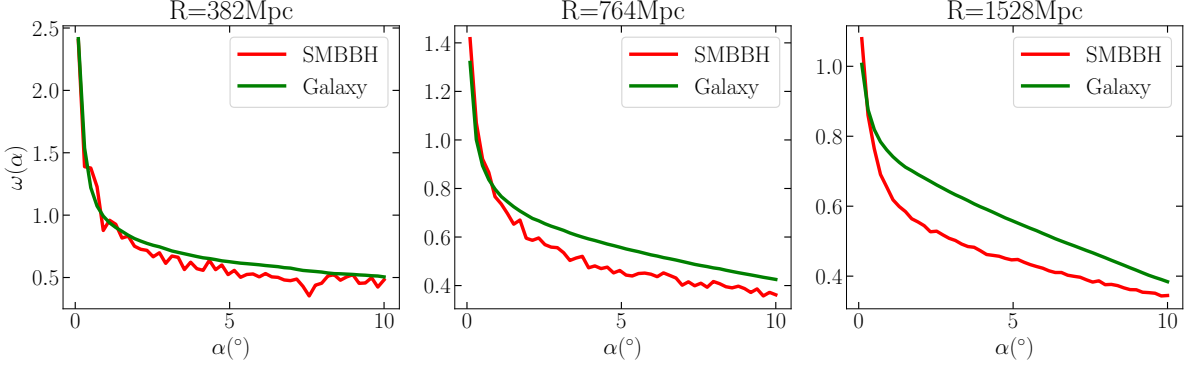


Figure 15. The two-point correlation functions ω of galaxies and SMBBHs as a function of $\alpha(^{\circ})$ for spherical shells with radius $R = 382, 764$ and 1528 respectively (from left to right).

1286 individual GW sources with SNR $\rho > 8$ during 20 years' observation time, while SKA-PTA is expected to identify 22695 individual GW sources with the same observation duration (See also [Chen et al. 2023](#). The ranges predicted by this paper cover our results).

The statistical distribution of SNRs of all individual GW sources for CPTA (red) and SKA-PTA (green) are shown in Figure 17. Their SNR distribution basically follow power law distribution. From the figure, one can observe the highest achievable SNR for the most optimistic individual cases. CPTA is capable of detecting individual sources with an SNR of over 100. Meanwhile, SKA-PTA, with its advanced sensitivity, is expected to detect GW sources with SNR values reaching more than 700.

Based on these resolvable individual GW sources by future PTAs, we can again use spherical harmonic expansion to analyze the angular power spectrum relating to their number density distributions across the celestial sphere. Since the number of detectable individual GW sources for CPTA is rather limited, we mainly focus on the individual GW sources that are detectable by SKA-PTA. We further plotted their two dimensional angular distribution sky map in Figure 19, and the result, i.e., the C_l 's as a function of l , are shown in Figure 21.

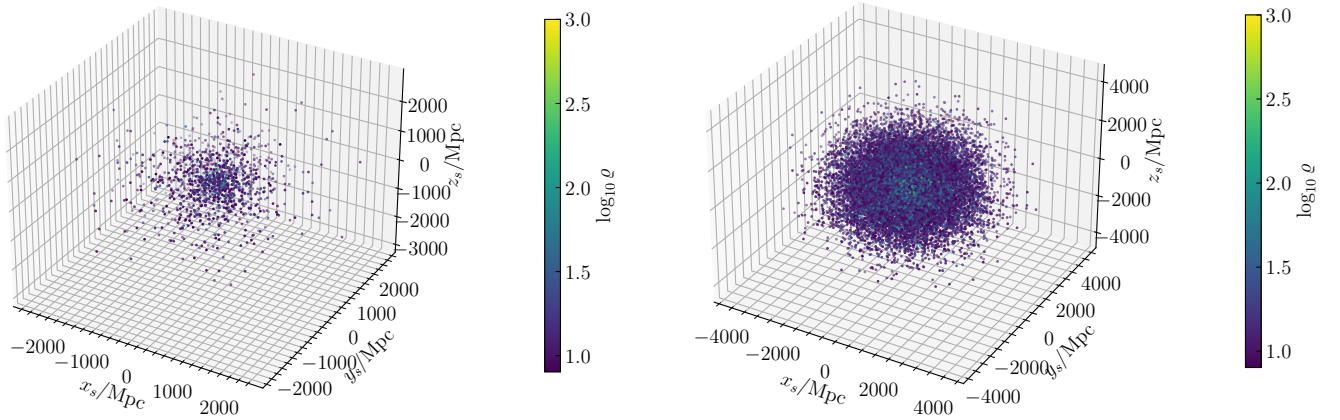


Figure 16. The three dimensional spatial distribution of GW sources detectable by CPTA (left) and SKA-PTA (right), where colors represent the logarithmic SNR, i.e., $\log_{10}(\rho)$, of each GW source.

4.2. Angular Resolution

In order to probe the large scale structure through GW signal from SMBBHs, we could have two distinct methodological options: one approach is to detect the GWB signal and study its anisotropy, while the other one involves the detection of a multitude of individual sources with enough SNR and high precision locations, so that sky map of these

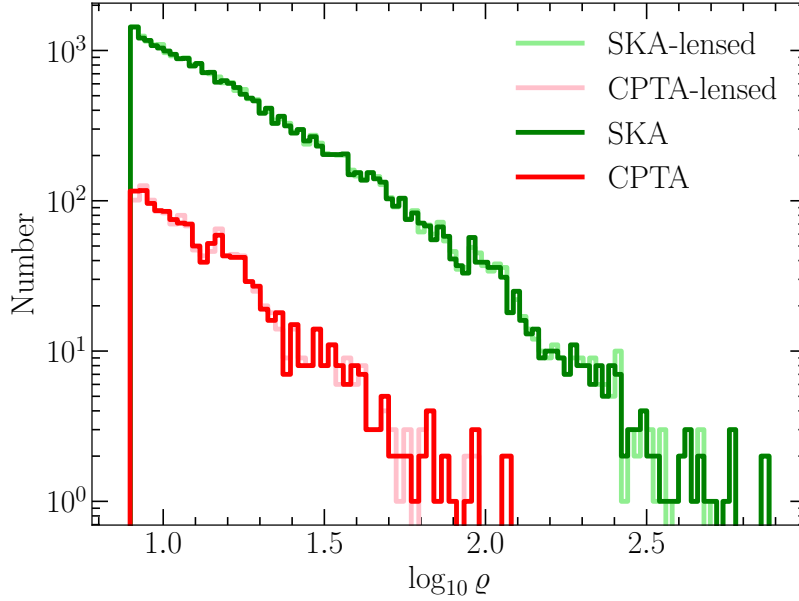


Figure 17. The logarithmic SNR distribution of individual GW sources for CPTA (red) and SKA-PTA (green). The distribution of SNR after considering the lensing effect is also shown as light red and light green lines.

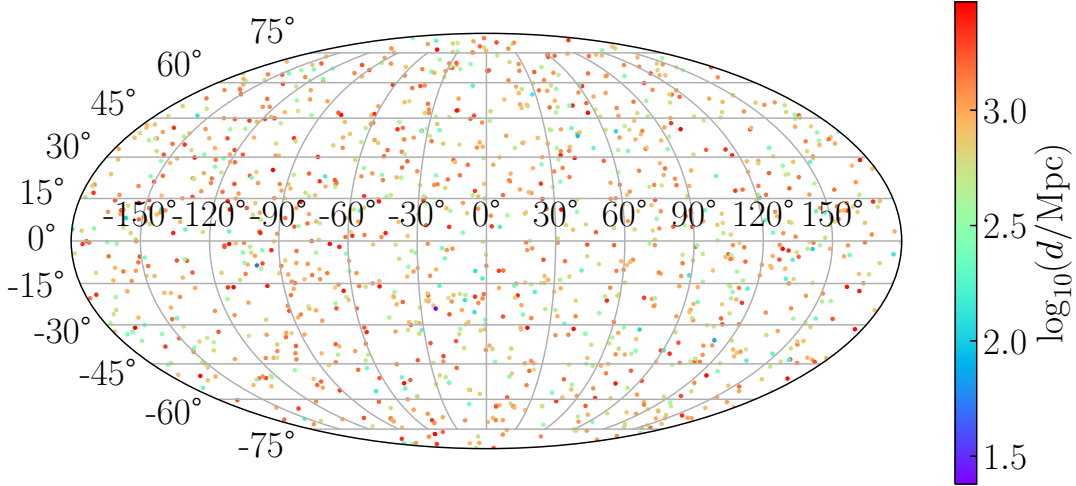


Figure 18. The angular position distribution sky map of individual GW sources detectable by CPTA, where colors represent the comoving distance to us.

individual sources can be constructed to study the underlying cosmic structures. As discussed in Guo et al. (2022) (see also Lee et al. 2011), it is possible that, under ideal conditions and with the incorporation of pulsar terms, PTAs utilizing a substantial ensemble of MSPs may achieve a localization precision as fine as 1° , thus the second approach for the detection of large-scale structures is anticipated to be within reach in the future.

5. LENSING EFFECT

The gravitational wave signals from distant SMBBHs may be affected by the lensing effects of foreground galaxies or dark matter halos as they propagate towards Earth. In this section, we will discuss whether the gravitational lensing effect will have a significant impact on the various results related to GWB and individual sources that we have derived in previous sections. We adopt the lensing model used in Oguri (2018), where they developed a hybrid framework to compute the magnification probability distribution function (PDF) that takes into account both weak and strong gravitational lensing effect for wide ranges of source redshifts and magnifications. We randomly assigned

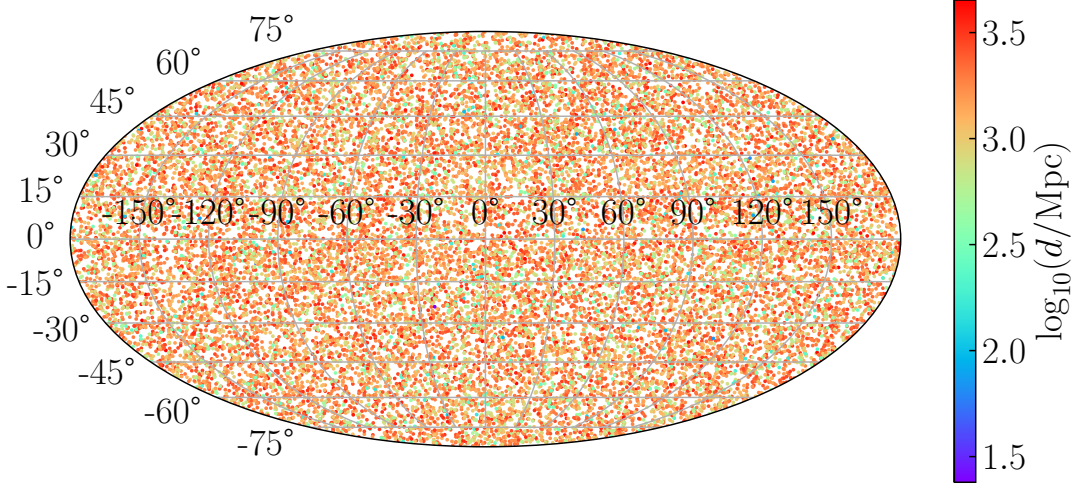


Figure 19. The angular position distribution sky map of individual GW sources detectable by SKA-PTA, where colors represent the comoving distance to us.

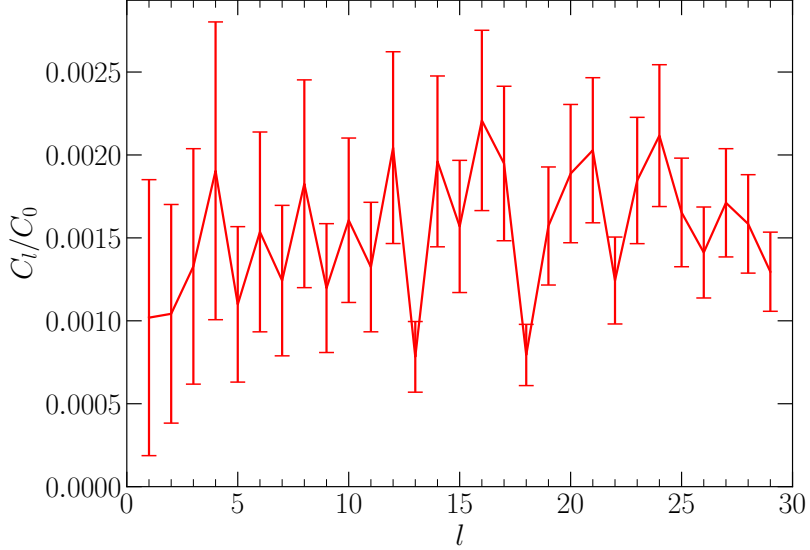


Figure 20. Angular power spectrum coefficients C_l as a function of l for the number density of the GW sources detectable by CPTA, where error bar indicate the cosmic variance.

a magnification factor $\sqrt{\mu}$ to each gravitational wave event amplitude h_i according to the PDF under this model. We compare the results with and without lensing effect in the following subsection.

5.1. Results

From Figure 22 we can see that, for the characteristic amplitude of the GWB, upon incorporating the lensing effect into our calculations, we observed a subtle change in the characteristic amplitude of GWB. Specifically, the amplitude exhibited a slight increase at the order of 10^{-17} , which is one to three order of magnitude smaller than the value of the amplitude itself. This increase is sufficiently small that it does not significantly alter the overall behavior of the GWB signal. For the anisotropy property of the GWB signal, lensing effects induced variation of the C_l coefficients is roughly within two percent of the original value, the effect of gravitational lensing is not significant either.

For the detectability of individual sources, after incorporating the lensing effect, the number of resolvable individual sources for SKA increased from 22,695 to 22,828, and for CPTA, it increased from 1,286 to 1,287. This indicates an overall increasing trend, although the increase accounts for only a small fraction. The distribution of the SNR also

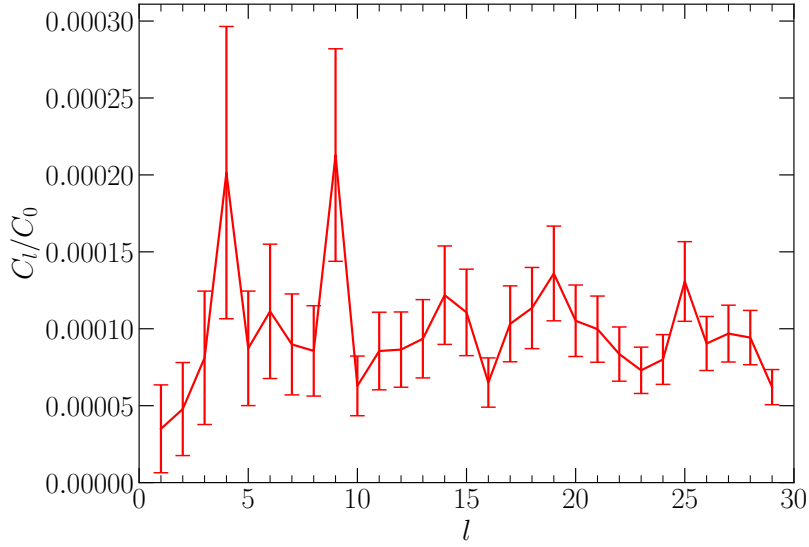


Figure 21. Angular power spectrum coefficients C_l as a function of l for the number density of the GW sources detectable by SKA-PTA, where error bar indicate the cosmic variance.

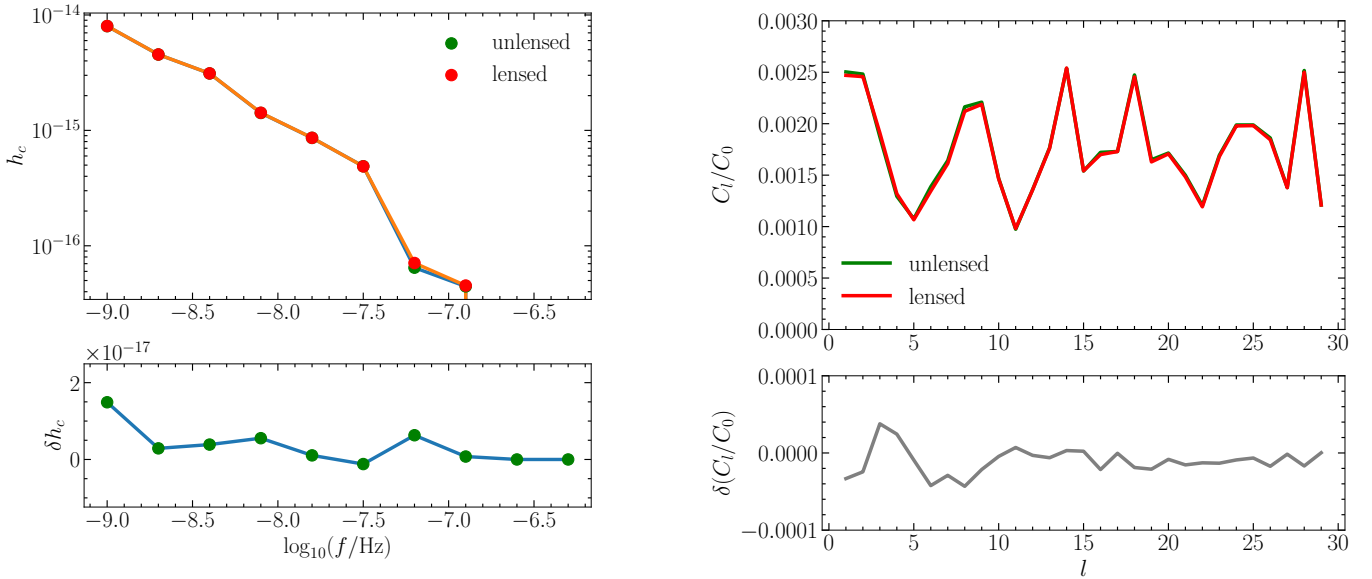


Figure 22. A comparison of the isotropic and anisotropic properties of the GWB with and without considering gravitational lensing effects. Left panel: comparison of the GWB characteristic amplitude and spectrum (upper panel) and their difference (lower panel), lensing effects induced variation is one to three order of magnitude smaller than the original value; Right panel: comparison of the C_l coefficients (upper panel) and their differences (lower panel), lensing effects induced variation is one order of magnitude smaller than the original value.

shows only a subtle impact due to the lensing effect. This suggests that while gravitational lensing does have an influence on the detection of gravitational wave sources, its effect on the overall observability and SNR distribution is rather limited. In Figure 17, we present a comparison of the SNR distributions with and without the lensing effect, where lighter colors illustrate the distribution of SNR after considering the lensing effect.

6. CONCLUSIONS AND DISCUSSION

Utilizing data from numerical cosmological simulation, we generated more than 3×10^7 SMBBHs distributed in the observable universe as GW sources of PTA. While maintaining the features of cosmic large-scale structure in the mock universe, we studied the isotropic and anisotropic characteristics of SMBBH sources and GWB signal, predicted the properties of detectable individual GW sources by CPTA and SKA-PTA, and also examined the influence of gravitational lensing effects.

For GWB, we calculated its characteristic amplitude and spectrum, and found that the resulting GWB signal has an amplitude $A \approx 4.85 \times 10^{-16}$ at the characteristic frequency yr^{-1} . We demonstrated the anisotropy properties in the distribution of simulated GW sources and the GWB signal using sky maps, and derived the angular power spectrum coefficients C_l as a function of l for the energy density of GWB. We predict that $C_1/C_0 \approx 2.50 \times 10^{-3} \pm 2.04 \times 10^{-3}$ and $C_2/C_0 \approx 2.48 \times 10^{-3} \pm 1.57 \times 10^{-3}$. For angular power spectrum in different frequency bins, C_l/C_0 at higher frequency end can even reach ~ 0.8 , while in the lower frequency end, C_l/C_0 generally ranges from 0.001 to 0.01 for $l > 0$. We investigated the clustering patterns of GW sources in spherical shells at various redshifts and discovered that, on relatively smaller scales, the clustering patterns of SMBBHs are more similar to that of galaxies. If integrated with data from stellar-mass black hole events, this approach holds the potential to more comprehensively reflect the cosmic large-scale structure. We also studied the detection capability of the future CPTA and SKA-PTA for individual sources. From our calculation results, we predict that CPTA is projected to detect 1286 individual GW sources with a SNR greater than 8 during 20 years' observation time, while SKA-PTA is projected to detect as many as 22695 individual GW sources, some of which may even achieve a SNR exceeding 700. These mock individual sources can provide more realistic samples to further study. Finally, we took gravitational lensing effects into account and found that lensing effects slightly enhanced our results, including the characteristic amplitude of the GWB signal and the number of detectable individual sources. However, overall, the impact is rather limited.

Below, we offer some further discussions. As was mentioned at the end of Section 3.2, our result of the GWB characteristic spectrum lies below the current experimental data points. This discrepancy may stem from several factors. One such factor is that SAM inevitable has its own uncertainties in its model construction. If we consider other versions of SAM that have slightly higher merger rates, e.g., Henriques2015 (Yang et al. 2019), it is still possible that SAM may offer results that is nearly compatible with observational data points. Furthermore, it is also possible that the GWB signal detected is a complex superposition of signals from multiple sources across the universe. While SMBBHs are known to be significant contributors to this background, they are not the sole constituents. Other astrophysical phenomena, such as binary white dwarf or the early universe's phase transition processes, may also imprint their signatures on the GWB, thereby complicating the interpretation of the observed signals and may also contribute to the discrepancy. However, it is important to emphasize that, despite these complexities, our current projected value of the GWB amplitude falls well within the theoretical range of $[1 \times 10^{-16}, 5 \times 10^{-15}]$ given by existing literature.

Since current N -body simulations combined with semi-analytical models cannot provide accurate information about the frequencies and orbits of SMBBH systems, we also made the simplifying assumption that the orbits of the SMBBHs are perfectly circular when calculating the frequency distribution probability and GW strains. If future numerical simulations can provide more detailed information on the orbital dynamics and evolution of SMBBHs, we will be able to develop more precise models for PTA band signal prediction. We will also update our results in future works based on certain orbital eccentricity assumptions.

We have theoretically explored the possibility of reconstructing the large-scale structure of the universe using super-massive black holes. But it is important to recognize that the individual sources detected by PTAs may be subject to observational biases. These sources are likely to be found in large elliptical galaxies, which could introduce bias compared to the general galaxy population (Chen et al. 2020). To effectively utilize these individual sources for investigating the large-scale structure of the universe, it is crucial to gain a clear understanding of this bias and to implement appropriate corrections within our observational methodologies.

It is also interesting to consider that the standard Hellings-Downs curve is derived on the assumption of an isotropic GWB (Hellings & Downs 1983), the presence of anisotropic components in the GWB could affect the angular correlation, causing it to deviate from the standard curve. It is possible that, based on our results, we can provide a description on HD curve's configuration under the influence of anisotropy. We leave this also to future work.

1 We thank Prof. Youjun Lu, Qi Guo, Chengliang Wei for helpful suggestions. Xiao Guo is supported by the Postdoctoral
 2 Fellowship Program and of China Postdoctoral Science Foundation under Grant Number BX20230104. We acknowledge
 3 the Beijing Super Cloud Computing Center for providing HPC resources that have contributed to the research results
 4 reported within this paper (URL: <http://www.blsc.cn/>).

REFERENCES

- Agazie, G., Anumarlapudi, A., Archibald, A. M., et al. 2023a, *ApJL*, 951, L8, doi: [10.3847/2041-8213/acdac6](https://doi.org/10.3847/2041-8213/acdac6)
 —. 2023b, *ApJL*, 952, L37, doi: [10.3847/2041-8213/ace18b](https://doi.org/10.3847/2041-8213/ace18b)
 —. 2023c, *ApJL*, 956, L3, doi: [10.3847/2041-8213/acf4fd](https://doi.org/10.3847/2041-8213/acf4fd)
 Antoniadis, J., Arumugam, P., Arumugam, S., et al. 2023, arXiv e-prints, arXiv:2306.16227, doi: [10.48550/arXiv.2306.16227](https://doi.org/10.48550/arXiv.2306.16227)
 Arzoumanian, Z., Baker, P. T., Blumer, H., et al. 2020, *ApJL*, 905, L34, doi: [10.3847/2041-8213/abd401](https://doi.org/10.3847/2041-8213/abd401)
 Barnes, J. E., & Hernquist, L. 1996, *ApJ*, 471, 115, doi: [10.1086/177957](https://doi.org/10.1086/177957)
 Barnes, J. E., & Hernquist, L. E. 1991, *ApJL*, 370, L65, doi: [10.1086/185978](https://doi.org/10.1086/185978)
 Bartolo, N., Bertacca, D., Caldwell, R., et al. 2022, *JCAP*, 2022, 009, doi: [10.1088/1475-7516/2022/11/009](https://doi.org/10.1088/1475-7516/2022/11/009)
 Blair, D., Ju, L., Zhao, C., et al. 2015, *Science China Physics, Mechanics, and Astronomy*, 58, 5748, doi: [10.1007/s11433-015-5748-6](https://doi.org/10.1007/s11433-015-5748-6)
 Blandford, R., Narayan, R., & Romani, R. W. 1984, *Journal of Astrophysics and Astronomy*, 5, 369, doi: [10.1007/BF02714466](https://doi.org/10.1007/BF02714466)
 Boyle, B. J., & Terlevich, R. J. 1998, *MNRAS*, 293, L49, doi: [10.1046/j.1365-8711.1998.01264.x](https://doi.org/10.1046/j.1365-8711.1998.01264.x)
 Brazier, A., Lassus, A., Petiteau, A., et al. 2016, *Monthly Notices of the Royal Astronomical Society*, 458, 1267, doi: [10.1093/mnras/stw347](https://doi.org/10.1093/mnras/stw347)
 Chen, Y., Yu, Q., & Lu, Y. 2020, *ApJ*, 897, 86, doi: [10.3847/1538-4357/ab9594](https://doi.org/10.3847/1538-4357/ab9594)
 —. 2023, *ApJ*, 955, 132, doi: [10.3847/1538-4357/ace59f](https://doi.org/10.3847/1538-4357/ace59f)
 Cornish, N. J., & Sesana, A. 2013, *Classical and Quantum Gravity*, 30, 224005, doi: [10.1088/0264-9381/30/22/224005](https://doi.org/10.1088/0264-9381/30/22/224005)
 Cornish, N. J., & van Haasteren, R. 2014, arXiv e-prints, arXiv:1406.4511, doi: [10.48550/arXiv.1406.4511](https://doi.org/10.48550/arXiv.1406.4511)
 Creighton, J., & Anderson, W. 2011, *Gravitational-Wave Physics and Astronomy: An Introduction to Theory, Experiment and Data Analysis*. (Wiley -VCH Verlag GmbH & Co. KGaA)
 Detweiler, S. 1979, *ApJ*, 234, 1100, doi: [10.1086/157593](https://doi.org/10.1086/157593)
 Di Matteo, T., Springel, V., & Hernquist, L. 2005, *Nature*, 433, 604, doi: [10.1038/nature03335](https://doi.org/10.1038/nature03335)
 EPTA Collaboration, InPTA Collaboration, Antoniadis, J., et al. 2023, *A&A*, 678, A50, doi: [10.1051/0004-6361/202346844](https://doi.org/10.1051/0004-6361/202346844)
 Ferrarese, L., & Merritt, D. 2000, *ApJL*, 539, L9, doi: [10.1086/312838](https://doi.org/10.1086/312838)
 Foster, R. S., & Backer, D. C. 1990, *ApJ*, 361, 300, doi: [10.1086/169195](https://doi.org/10.1086/169195)
 Guo, Q., White, S., Angulo, R. E., et al. 2013, *MNRAS*, 428, 1351, doi: [10.1093/mnras/sts115](https://doi.org/10.1093/mnras/sts115)
 Guo, Q., White, S., Boylan-Kolchin, M., et al. 2011, *MNRAS*, 413, 101, doi: [10.1111/j.1365-2966.2010.18114.x](https://doi.org/10.1111/j.1365-2966.2010.18114.x)
 Guo, X., Lu, Y., & Yu, Q. 2022, *ApJ*, 939, 55, doi: [10.3847/1538-4357/ac9131](https://doi.org/10.3847/1538-4357/ac9131)
 Guo, X., Yu, Q., & Lu, Y. 2024, arXiv e-prints, arXiv:2411.14150, doi: [10.48550/arXiv.2411.14150](https://doi.org/10.48550/arXiv.2411.14150)
 Hellings, R. W., & Downs, G. S. 1983, *ApJL*, 265, L39, doi: [10.1086/183954](https://doi.org/10.1086/183954)
 Henriques, B. M. B., White, S. D. M., Thomas, P. A., et al. 2015, *MNRAS*, 451, 2663, doi: [10.1093/mnras/stv705](https://doi.org/10.1093/mnras/stv705)
 Hernquist, L. 1989, *Nature*, 340, 687, doi: [10.1038/340687a0](https://doi.org/10.1038/340687a0)
 Hopkins, P. F., Hernquist, L., Cox, T. J., & Kereš, D. 2008, *ApJS*, 175, 356, doi: [10.1086/524362](https://doi.org/10.1086/524362)
 Hotinli, S. C., Kamionkowski, M., & Jaffe, A. H. 2019, *The Open Journal of Astrophysics*, 2, 8, doi: [10.21105/astro.1904.05348](https://doi.org/10.21105/astro.1904.05348)
 Jaffe, A. H., & Backer, D. C. 2003, *ApJ*, 583, 616, doi: [10.1086/345443](https://doi.org/10.1086/345443)
 Joshi, B. C., Arumugasamy, P., Bagchi, M., et al. 2018, *Journal of Astrophysics and Astronomy*, 39, 51, doi: [10.1007/s12036-018-9549-y](https://doi.org/10.1007/s12036-018-9549-y)
 Kelley, L. Z., Blecha, L., & Hernquist, L. 2017, *MNRAS*, 464, 3131, doi: [10.1093/mnras/stw2452](https://doi.org/10.1093/mnras/stw2452)
 Kormendy, J., & Ho, L. C. 2013, *ARA&A*, 51, 511, doi: [10.1146/annurev-astro-082708-101811](https://doi.org/10.1146/annurev-astro-082708-101811)
 Kormendy, J., & Richstone, D. 1995, *ARA&A*, 33, 581, doi: [10.1146/annurev.aa.33.090195.003053](https://doi.org/10.1146/annurev.aa.33.090195.003053)
 Kramer, M., & Champion, D. J. 2013, *Classical and Quantum Gravity*, 30, 224009, doi: [10.1088/0264-9381/30/22/224009](https://doi.org/10.1088/0264-9381/30/22/224009)
 Lazio, T. J. W. 2013, *Classical and Quantum Gravity*, 30, 224011, doi: [10.1088/0264-9381/30/i=22/a=224011](https://doi.org/10.1088/0264-9381/30/i=22/a=224011)
<http://stacks.iop.org/0264-9381/30/i=22/a=224011>

- Lee, K. J., Wex, N., Kramer, M., et al. 2011, *MNRAS*, 414, 3251, doi: [10.1111/j.1365-2966.2011.18622.x](https://doi.org/10.1111/j.1365-2966.2011.18622.x)
- Li, Z., Jiang, Z., Liu, Y., et al. 2024, arXiv e-prints, arXiv:2412.09956, doi: [10.48550/arXiv.2412.09956](https://doi.org/10.48550/arXiv.2412.09956)
- Madau, P., Ferguson, H. C., Dickinson, M. E., et al. 1996, *MNRAS*, 283, 1388, doi: [10.1093/mnras/283.4.1388](https://doi.org/10.1093/mnras/283.4.1388)
- Maggiore, M. 2008, *Gravitational waves: Volume 1: Theory and experiments* (Oxford: Oxford University Press)
- Magorrian, J., Tremaine, S., Richstone, D., et al. 1998, *AJ*, 115, 2285, doi: [10.1086/300353](https://doi.org/10.1086/300353)
- Manchester, R. N. 2013, *International Journal of Modern Physics D*, 22, 1341007, doi: [10.1142/S0218271813410071](https://doi.org/10.1142/S0218271813410071)
- Manchester, R. N., & IPTA. 2013, *Classical and Quantum Gravity*, 30, 224010, doi: [10.1088/0264-9381/30/22/224010](https://doi.org/10.1088/0264-9381/30/22/224010)
- McLaughlin, M. A. 2013, *Classical and Quantum Gravity*, 30, 224008, doi: [10.1088/0264-9381/30/22/224008](https://doi.org/10.1088/0264-9381/30/22/224008)
- Mihos, J. C., & Hernquist, L. 1994, *ApJL*, 431, L9, doi: [10.1086/187460](https://doi.org/10.1086/187460)
- . 1996, *ApJ*, 464, 641, doi: [10.1086/177353](https://doi.org/10.1086/177353)
- Miles, M. T., Shannon, R. M., Bailes, M., et al. 2023, *MNRAS*, 519, 3976, doi: [10.1093/mnras/stac3644](https://doi.org/10.1093/mnras/stac3644)
- Mingarelli, C. M. 2015, *Gravitational wave astrophysics with pulsar timing arrays* (Springer)
- Mingarelli, C. M. F., Sidery, T., Mandel, I., & Vecchio, A. 2013, *PhRvD*, 88, 062005, doi: [10.1103/PhysRevD.88.062005](https://doi.org/10.1103/PhysRevD.88.062005)
- Nan, R., Li, D., Jin, C., et al. 2011, *International Journal of Modern Physics D*, 20, 989, doi: [10.1142/S0218271811019335](https://doi.org/10.1142/S0218271811019335)
- Oguri, M. 2018, *Mon. Not. Roy. Astron. Soc.*, 480, 3842, doi: [10.1093/mnras/sty2145](https://doi.org/10.1093/mnras/sty2145)
- Perera, B. B. P., DeCesar, M. E., Demorest, P. B., et al. 2019, *MNRAS*, 490, 4666, doi: [10.1093/mnras/stz2857](https://doi.org/10.1093/mnras/stz2857)
- Ransom, S., Brazier, A., Chatterjee, S., et al. 2019, in *Bulletin of the American Astronomical Society*, Vol. 51, 195. <https://arxiv.org/abs/1908.05356>
- Reardon, D. J., Zic, A., Shannon, R. M., et al. 2023, *ApJL*, 951, L6, doi: [10.3847/2041-8213/acdd02](https://doi.org/10.3847/2041-8213/acdd02)
- Sah, M. R., & Mukherjee, S. 2024, arXiv e-prints, arXiv:2407.11669, doi: [10.48550/arXiv.2407.11669](https://doi.org/10.48550/arXiv.2407.11669)
- Sah, M. R., Mukherjee, S., Saeedzadeh, V., et al. 2024, *MNRAS*, 533, 1568, doi: [10.1093/mnras/stae1930](https://doi.org/10.1093/mnras/stae1930)
- Sanders, D. B., Soifer, B. T., Elias, J. H., et al. 1988, *ApJ*, 325, 74, doi: [10.1086/165983](https://doi.org/10.1086/165983)
- Sathyaprakash, B. S., & Schutz, B. F. 2009, *Living Reviews in Relativity*, 12, 2, doi: [10.12942/lrr-2009-2](https://doi.org/10.12942/lrr-2009-2)
- Sato-Polito, G., & Kamionkowski, M. 2024, *PhRvD*, 109, 123544, doi: [10.1103/PhysRevD.109.123544](https://doi.org/10.1103/PhysRevD.109.123544)
- Sazhin, M. V. 1978, *Soviet Ast.*, 22, 36
- Schutz, K., & Ma, C.-P. 2016, *MNRAS*, 459, 1737, doi: [10.1093/mnras/stw768](https://doi.org/10.1093/mnras/stw768)
- Sesana, A. 2013a, *Classical and Quantum Gravity*, 30, 244009, doi: [10.1088/0264-9381/30/24/244009](https://doi.org/10.1088/0264-9381/30/24/244009)
- . 2013b, *MNRAS*, 433, L1, doi: [10.1093/mnrasl/slt034](https://doi.org/10.1093/mnrasl/slt034)
- Sesana, A. 2015, in *Astrophysics and Space Science Proceedings*, Vol. 40, *Gravitational Wave Astrophysics*, 147, doi: [10.1007/978-3-319-10488-1_13](https://doi.org/10.1007/978-3-319-10488-1_13)
- Sesana, A., Shankar, F., Bernardi, M., & Sheth, R. K. 2016, *MNRAS*, 463, L6, doi: [10.1093/mnrasl/slw139](https://doi.org/10.1093/mnrasl/slw139)
- Sesana, A., & Vecchio, A. 2010, *Classical and Quantum Gravity*, 27, 084016, doi: [10.1088/0264-9381/27/8/084016](https://doi.org/10.1088/0264-9381/27/8/084016)
- Sesana, A., Vecchio, A., & Volonteri, M. 2009, *MNRAS*, 394, 2255, doi: [10.1111/j.1365-2966.2009.14499.x](https://doi.org/10.1111/j.1365-2966.2009.14499.x)
- Shao, X., Cao, Z., Fan, X., & Wu, S. 2022, *Research in Astronomy and Astrophysics*, 22, 015006, doi: [10.1088/1674-4527/ac32b4](https://doi.org/10.1088/1674-4527/ac32b4)
- Smits, R., Lorimer, D. R., Kramer, M., et al. 2009, *A&A*, 505, 919, doi: [10.1051/0004-6361/200911939](https://doi.org/10.1051/0004-6361/200911939)
- Soltan, A. 1982, *MNRAS*, 200, 115, doi: [10.1093/mnras/200.1.115](https://doi.org/10.1093/mnras/200.1.115)
- Springel, V., White, S. D. M., Jenkins, A., et al. 2005, *Nature*, 435, 629, doi: [10.1038/nature03597](https://doi.org/10.1038/nature03597)
- Taylor, S., Burke-Spolaor, S., Baker, P. T., et al. 2019, *BAAS*, 51, 336. <https://arxiv.org/abs/1903.08183>
- Taylor, S. R., & Gair, J. R. 2013, *PhRvD*, 88, 084001, doi: [10.1103/PhysRevD.88.084001](https://doi.org/10.1103/PhysRevD.88.084001)
- Taylor, S. R., Mingarelli, C. M. F., Gair, J. R., et al. 2015, *PhRvL*, 115, 041101, doi: [10.1103/PhysRevLett.115.041101](https://doi.org/10.1103/PhysRevLett.115.041101)
- Treister, E., Schawinski, K., Urry, C. M., & Simmons, B. D. 2012, *ApJL*, 758, L39, doi: [10.1088/2041-8205/758/2/L39](https://doi.org/10.1088/2041-8205/758/2/L39)
- Ueda, Y., Akiyama, M., Ohta, K., & Miyaji, T. 2003, *ApJ*, 598, 886, doi: [10.1086/378940](https://doi.org/10.1086/378940)
- van Haasteren, R. 2014, *Gravitational Wave Detection and Data Analysis for Pulsar Timing Arrays* (Springer)
- Wang, Y., & Mohanty, S. D. 2017, *Physical Review Letters*, 118, 151104, doi: [10.1103/PhysRevLett.118.151104](https://doi.org/10.1103/PhysRevLett.118.151104)
- Xu, H., Chen, S., Guo, Y., et al. 2023, *Research in Astronomy and Astrophysics*, 23, 075024, doi: [10.1088/1674-4527/acdfa5](https://doi.org/10.1088/1674-4527/acdfa5)
- Yang, Q., Hu, B., & Li, X.-D. 2019, *MNRAS*, 483, 503, doi: [10.1093/mnras/sty3126](https://doi.org/10.1093/mnras/sty3126)
- Yu, Q., & Tremaine, S. 2002, *MNRAS*, 335, 965, doi: [10.1046/j.1365-8711.2002.05532.x](https://doi.org/10.1046/j.1365-8711.2002.05532.x)
- Zheng, X. Z., Bell, E. F., Somerville, R. S., et al. 2009, *ApJ*, 707, 1566, doi: [10.1088/0004-637X/707/2/1566](https://doi.org/10.1088/0004-637X/707/2/1566)
- Zheng, Y., Kouvatsos, N., Golomb, J., et al. 2023, *PhRvL*, 131, 171403, doi: [10.1103/PhysRevLett.131.171403](https://doi.org/10.1103/PhysRevLett.131.171403)

Zhu, X. J., Hobbs, G., Wen, L., et al. 2014, MNRAS, 444,
3709, doi: [10.1093/mnras/stu1717](https://doi.org/10.1093/mnras/stu1717)